

Dirac fermions in the altermagnet Ce_4Sb_3

Xue He and Shihao Zhang*

School of Physics and Electronics, Hunan University, Changsha 410082, China

Altermagnetism exhibits zero net magnetization and spin-splitting electronic structure. The interplay between altermagnetism and topological physics becomes an important topic in the condensed matter physics. In this letter, we propose that the altermagnet Ce_4Sb_3 hosts Dirac fermions through first-principles calculations and tight-binding model analysis. When subjected to external magnetic field, the altermagnet Ce_4Sb_3 change from altermagnetic state to ferromagnetic state. Accompanied with magnetic order transition, the four-fold degenerate Dirac points are transited into sextuple degenerate points. Especially, spin-orbital coupling effect has little influence about the Dirac fermions. The topological phases in the altermagnetic state may hold the exotic spin-splitter torque and remarkable nonlinear transport effect. Our work paves the way for exploring the interplay between altermagnetism and non-trivial topological phase.

Recently, altermagnetism has emerged as a significant topic in the condensed matter physics[1–13]. The altermagnetism exhibits zero net magnetization akin to antiferromagnetism. However, the sublattices with opposite spin can not be interconverted by translation or inversion symmetry, resulting in a broken Kramers degeneracy that gives rise to a spin-split electronic structure. Several materials exhibit this collinear compensated magnetic order, such as RuO_2 [1, 14–19], MnF_2 [20–22], FeSb_2 [23], CrSb [24–26], $\kappa\text{-Cl}$ [27, 28], Cr_2SO [29], RuF_4 [30, 31], LaMnO_3 [13] and $\text{V}_2\text{Se}_2\text{O}$ [32, 33]. In these altermagnets, different sublattices are connected by rotational symmetry, and the energy bands display spin-splitting characteristics even without requiring spin-orbital coupling. Due to their distinctive electronic structure, altermagnetism showcases various novel physical phenomena, including the crystal Hall effect [34–41], spin currents [42–48], crystal thermal transport [49, 50], magneto-optical Kerr effect[51] and spin-splitting torque effects [52, 53].

Moreover, the altermagnetism can coexist with other novel electronic order. The altermagnet LiFe_2F_6 is theoretically found to host the ferroelectric order and possible spin-triplet exciton state[54]. And the altermagnetism can introduce the finite-momentum Cooper pair and Majorana zero mode in the heterostructure[55]. Thus, the interplay between altermagnetism and topological electron has garnered significant public interest. By employing effective models and symmetric analysis, researchers have explored the Weyl nodals and mirror Chern bands in the altermagnet[56]. However, the study about the material realization of altermagnet featuring non-trivial topological properties remained scarce yet.

In this letter, we propose that the metallic altermagnet Ce_4Sb_3 exhibits the non-trivial topological phase. The first-principles calculations, symmetry analysis and tight-binding model demonstrated that there are Dirac fermions in the altermagnetic state. Under external magnetic field, the altermagnetic order is transited into ferromagnetic order. In the ferromagnetic state, there are six-fold degenerate points protected by C_3 rotational symmetry. Thus, an external magnetic field can trigger the mag-

netic order transition, leading to a resultant topological transition. Different from Dirac fermions in the conventional antiferromagnets without spin splitting electronic structures[57], the Dirac fermions in the altermagnetic state can give rise to enhanced spin-splitter torque and notable nonlinear transport effect.

The metallic compound Ce_4Sb_3 exhibits a cubic structure reminiscent of Th_3P_4 -type belonging to the space group $I\bar{4}3d$ (No. 220). Its noncentrosymmetric unit cell is illustrated in Fig.1(a). The primitive cell of Ce_4Sb_3 comprises eight Ce and six Sb atoms, whose lattice constant is $\sqrt{3}a = 8.316\text{\AA}$ as depicted in Fig.1(a). Our Bader charge analysis reveal two species of spins of Ce atoms lost 0.73 and 0.64 electrons per atom, respectively, and six Sb atoms gain 0.9 electrons on average per atom. Each Ce atom has three nearest neighboring Ce atoms and each atom carries $\sim 1\mu_B$ magnetic moment. The magnetic properties of the Ce_4Sb_3 compound is unconventional, which is known to exhibit ground-state ferromagnetic (FM) state with possible Kondo interaction[60]. However, recent neutron diffraction has unveiled a commensurate antiferromagnetic (AFM) arrangement in bulk Ce_4Sb_3 at 2K in the absence of a magnetic field [58, 59]. The ground magnetic structure of Ce_4Sb_3 bulk is shown in the Fig.1(b)[58, 59] and Table. S1, whose magnetic space group is No. 122.336 ($I\bar{4}'2d'$). And the spin space group of altermagnetic spin configuration is $I^{-1}\bar{4}^{-1}2^1d^{\text{inf}m}1$ [6, 7].

Our first-principles calculations reveal that AFM ground state become the ground state while on-site Hubbard parameter of Ce atoms' f orbital is set to $U = 1 \sim 3$ eV as shown in the Table. S2. We also performed the calculations about Hubbard parameter with linear response method[61], and our results show that self-consistent Hubbard parameter is 3.698 eV for Ce atoms' f orbitals. The metallic electronic structure provides strong screening effect due to virtual excitation of particle-hole pair in the Ce_4Sb_3 , which lead to the small Hubbard value of f-electrons.

To understand the magnetism of Ce_4Sb_3 , we calculated different exchange couplings between Ce atoms as shown

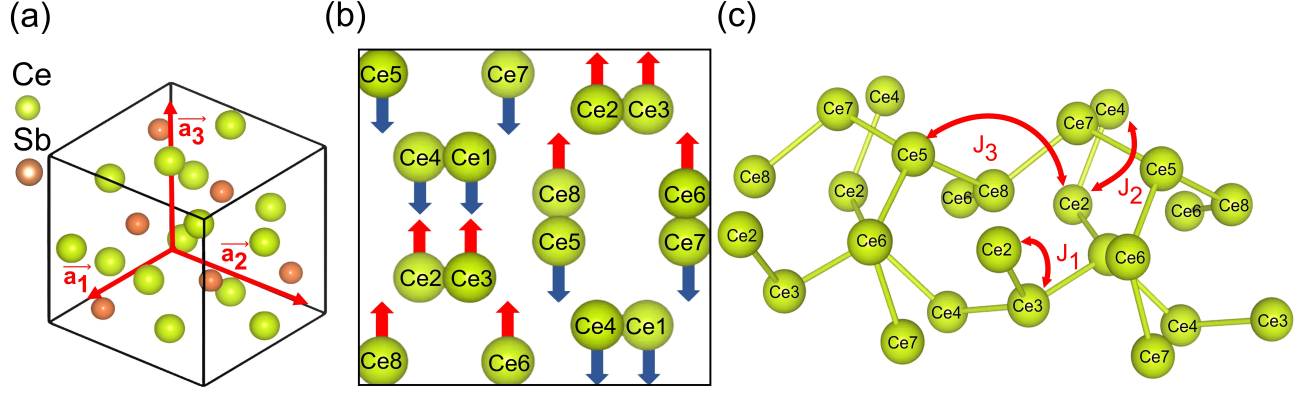


FIG. 1. (a) The primitive cell of the Ce_4Sb_3 compound. The basis vectors of primitive cell are $\mathbf{a}_1 = (-a, a, a)$, $\mathbf{a}_2 = (a, -a, a)$, $\mathbf{a}_3 = (a, a, -a)$. The lattice constant is $\sqrt{3}a = 8.316\text{\AA}$. (b) The spin configuration of Ce_4Sb_3 at 2K in the zero field[58, 59]. Only Ce atoms are shown and the Ce atomic indices are remarked in the figure. Here we adopt the supercell model for clarity. (c) The illustration about main magnetic exchange couplings. The nearest neighboring exchange coupling is given by $J_1 = 2.4781\text{ meV}$ which prefers to ferromagnetic couplings. And next nearest neighboring exchange interaction whose Ce atoms' distance is 3.715 \AA , is $J_2 = 0.2217\text{ meV}$. Additionally, the exchange interaction at a distance of 8.178\AA is given by $J_3 = -0.1777\text{ meV}$, which prefers to antiferromagnetic couplings.

in Fig. 1(c). We note that the competition between ferromagnetic coupling J_2 and antiferromagnetic coupling J_3 may lead to the low-temperature magnetic transition between AFM and FM states.

Now we discuss the electronic structure of Ce_4Sb_3 bulk. In the nonmagnetic and ferromagnetic cases, the Ce_4Sb_3 bulk obeys the T_d point group which lacks inversion symmetry, whereas in the antiferromagnetic state, the point group is reduced into the D_{2d} point group. The electronic structures of both ferromagnetic (FM) and antiferromagnetic (AFM) cases in the Ce_4Sb_3 bulk material are illustrated in the Fig.2. In the AFM ground state, the absence of inversion symmetry leads to broken Kramers symmetry, resulting in the altermagnetic energy bands, as depicted in the Fig.2(a). These electronic bands exhibit Dirac fermions near the Fermi level at six H points in the entire Brillouin zone as shown in the Fig.S2, which reveals the nontrivial topological electronic phases in the AFM state. The Dirac fermions are not sensitive to Hubbard parameters, and they also exist in the altermagnet Ce_4As_3 and Ce_4Bi_3 as shown in the Fig.S3-5. The AFM spin configuration is hold within the primitive cell, thus the band folding affect can be ruled out here. Near the Dirac point located at H_x ($\pm\pi/a, 0, 0$) point, the spin splitting is proportional to $(k_x^2 - k_z^2)(k_y - k_z)$, which becomes $\sim (k_y^2 - k_z^2)(k_x - k_z)$ near the Dirac point located at H_y ($0, \pm\pi/a, 0$) point. But near the Dirac point located at H_z ($0, 0, \pm\pi/a$) point, the spin splitting becomes $\sim (k_x^2 - k_z^2)(k_y^2 - k_z^2)$.

We focus on the crucial symmetry protecting the band topology in the altermagnet Ce_4Sb_3 . Near the Fermi level, the energy bands are mainly contributed by d orbitals of Ce atoms as shown in the Fig.S6. Along the $\Gamma - H$

direction, there exists a complex symmetry $\{C_{2y}\tau_x|\mathcal{T}\}$ where C_{2y} , τ_x and \mathcal{T} refer to two-fold rotational operation, sliding operation and time reversal operation, respectively. Under $\{C_{2y}\tau_x|\mathcal{T}\}$ symmetric operation, (x, y, z) becomes $(-x - 1/2, y, -z)$, and the $\{C_{2y}\tau_x|\mathcal{T}\}$ symmetry holds the degeneracy between energy bands of different spins. As for the high-symmetric reciprocal path along $H - N$ direction, the symmetry becomes $\{M_{yz}C_{4z}\tau'\}$. Here M_{yz} and C_{4z} represents the mirror operation and four-fold rotational operation, respectively. And $\tau' = (-1/4, 1/4, -1/4)$ describes the sliding operation. Under $\{M_{yz}C_{4z}\tau'\}$ operation, (x, y, z) becomes $(-y - 1/4, -x + 1/4, z - 1/4)$. As shown by detailed analysis in the supplementary materials, the $\{M_{yz}C_{4z}\tau'\}$ symmetry hold the double orbital degeneracy but lifts the spin degeneracy in the $H - N$ direction. Thus, the Dirac point in the altermagnetic state shown in the Fig.2 is protected by $\{M_{yz}C_{4z}\tau'\}$ and $\{C_{2y}\tau_x|\mathcal{T}\}$ symmetry.

Under external magnetic field, the Ce_4Sb_3 bulk undergoes a magnetic order transition, and ferromagnetic state becomes its ground state. The spin-up energy bands near the Fermi level mainly originates from f-orbitals of Ce atoms. These electrons experience strong interaction, potentially leading to a significant Kondo effect observed in previous experiments. On the other hand, the spin-down electronic structure is mainly contributed by the d-orbitals of Ce atoms. Due to the C_3 three-fold rotational symmetry, the energy bands exhibit sixfold degenerate points with high dispersion in the same spin channel, as shown in Fig.2(b). Thus, the magnetic field can transit the altermagnetic state into the ferromagnetic state with high topological charge, which may trigger a noteworthy circular photogalvanic effect.

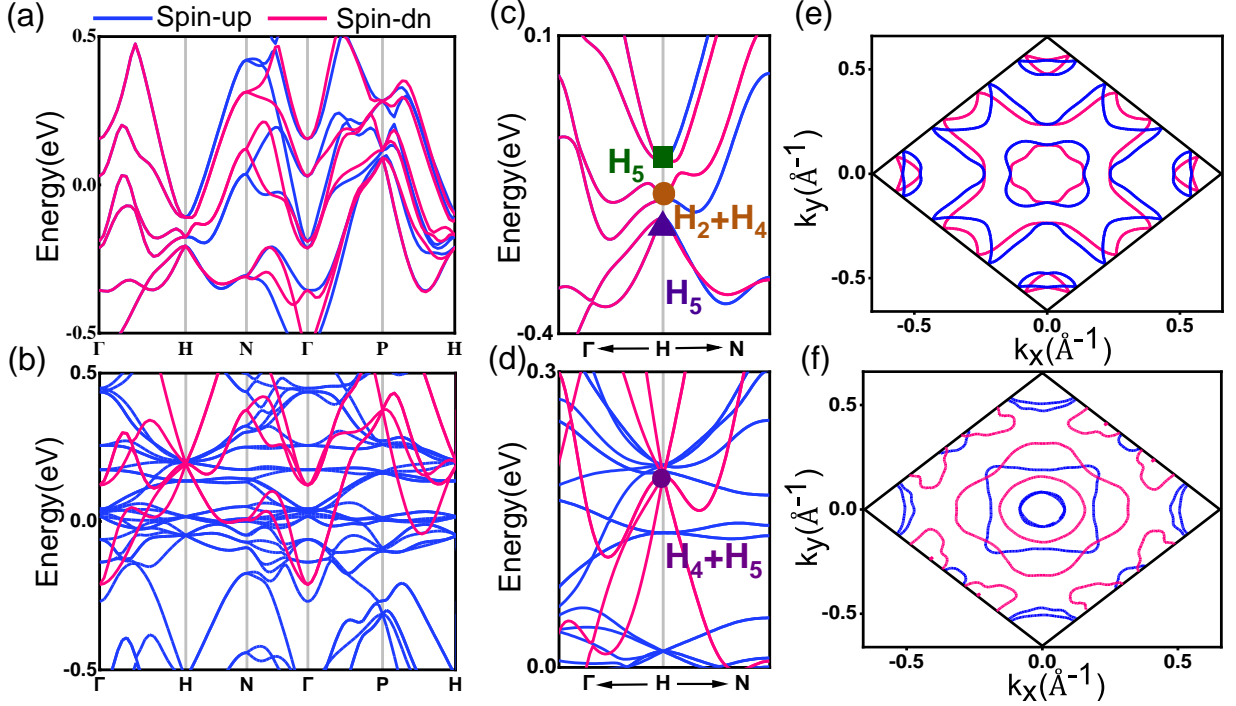


FIG. 2. The calculated electronic band structure and Fermi surfaces of the Ce_4Sb_3 compound with $U = 2$ eV without spin-orbit coupling (SOC) effect. Here the blue lines represent the spin-up bands and the red lines represent the spin-down energy bands. The band structure of the AFM state (a) and the energy bands of the FM state (b) are shown in the figure. Here H point is adopted as H_y point $(0, \pi/a, 0)$. (c) The zoom-in energy bands of AFM state near the Dirac points. (d) The zoom-in electronic structure of FM state near the sextuple degenerate points. The character table of point group D_{2d} is shown in the Table.S3. The $k_x - k_y$ Fermi surfaces of AFM states (e) and FM states (f) are also shown.

To gain insights into the topological electronic structure, we construct a 16-band tight-binding model based on the eight Ce atom considering spin degree. Each Ce atom possesses an on-site energy of E_0 , with hopping parameter of t between adjacent Ce atoms. In the paramagnetic phase, the model exhibits a 12-fold degenerate solution at $E_0 + t$ and a 4-fold degenerate solution at $E_0 - 3t$ at the H points. However, in the magnetic phase, Zeeman splitting $\pm m$ arises in different Ce sublattices. In the ferromagnetic phase, the solutions at the H point manifest as two 6-fold degenerate solutions $E_0 + t \pm m$ and two 2-fold degenerate solutions $E_0 - 3t \pm m$. In the antiferromagnetic phase, the solutions evolve into four Dirac points as

$$\begin{aligned}
 E_1 &= E_0 - t + \sqrt{m^2 + 4t^2} \quad (4\text{-fold}) \\
 E_2 &= E_0 - t - \sqrt{m^2 + 4t^2} \quad (4\text{-fold}) \\
 E_3 &= E_0 + t + m \quad (4\text{-fold}) \\
 E_4 &= E_0 + t - m \quad (4\text{-fold})
 \end{aligned} \tag{1}$$

Especially, as shown in the Fig.2(c), the orbital doublets in the antiferromagnetic state can be classified into $H_2 + H_4$ and H_5 representations. The wavefunctions of $H_2 + H_4$ representation keep unchanged under C_2 operation, but those of H_5 representation will flip their phase

under C_2 operation.

We also show the Fermi surface of AFM and FM states in the Fig.2(e,f). The FM Fermi surface exhibits the highly spin-polarization. But the AFM Fermi surface in the $k_x - k_y$ plane holds the d-wave magnetism without relativistic effect, where spin splitting is proportional to $\cos k_x - \cos k_y$. It may provide the finite-momentum Cooper pair and induce the unconventional proximitized superconductivity.

Spin-orbital coupling (SOC) effect always play an important role in the different systems. For example, when SOC effect is taken into consideration, the electronic structure of some altermagnets RuF_4 is dramatically influenced by SOC effect [30]. The calculated bands with SOC effect are present in the Fig. 3. In the FM state, due to the strong hybridization between d-orbitals and f-orbitals of opposite spins, the 6-fold degenerate points is fully destroyed in the FM state. In the AFM state, the SOC effects break the aforementioned $\{M_{yz}C_{4z}\tau'\}$ and $\{C_{2y}\tau_x|\mathcal{T}\}$ symmetry. There is no remarkable canted magnetic moment in the magnetic ground state, which implies the nonexistence of topological Hall effect. But the energy splitting near the Dirac point is very slight as shown in the Fig.3(a). The Dirac point is mainly contributed by d_{xz} and d_{z^2} orbitals, and little d_{yz} orbital

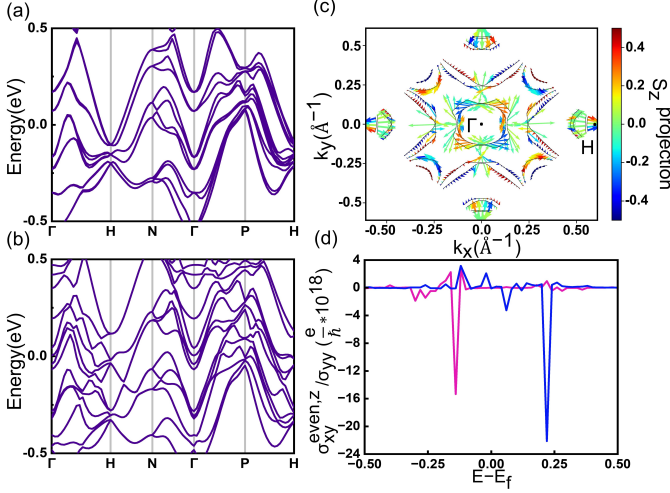


FIG. 3. The calculated SOC band structure and spin texture of the Ce_4Sb_3 compound with $U=2\text{ eV}$. (a) The band structure of the AFM state. (b) The energy bands of the FM state. (c) The spin texture in the $k_x - k_y$ plane, in which color depicts the spin projection of S_z component. (d) \mathcal{T} -even charge-spin conversion ratio $\sigma_{xy}^{\text{even},z}/\sigma$. Here the blue lines and red lines represent the $\sigma_{xy}^{\text{even},z}/\sigma$ in the CrSb [62] and that in the Ce_4Sb_3 with the SOC effect, respectively. The Weyl fermions in the CrSb is located near the 0.25 eV.

contributes to Dirac fermions. Thus, the Dirac fermions in the altermagnetic state still can be regarded as nearly degenerate electronic structure even under SOC effect, in which weak splitting originates from little weight of $\langle d_{xz}|L_z S_z|d_{yz}\rangle$ SOC matrix element. Thus, our results prove that the Dirac fermions in the altermagnetic state can be observed in the ARPES experiments.

Near the Dirac point, two energy bands have the in-plane spin texture structure under SOC effect as shown in the Fig.3(c). But the other two energy bands exhibit the k -dependent out-of-plane magnetization. The novel spin textures of four energy bands are attributed by topological electronic structure. We use a minimal model to describe this spin structure near the Dirac point. The SOC Hamiltonian in the first order of \mathbf{k} can be written as $H = k_x s_x \sigma_0 + k_y s_y \sigma_0 + k_x s_x \sigma_x + k_y s_y \sigma_x$ where s and σ refer to the Pauli matrices in the spin and orbital space. By solving this minimal model, we can obtain that two bands with in-plane spin texture and other two bands with out-of-plane collinear spin configuration. The out-of-plane collinear spin configuration is corrected to partially in-plane spin structure by SOC term of high order in \mathbf{k} . The SOC term can provide the non-zero Berry curvature $\mathbf{\Omega}(\mathbf{k})$ near the Dirac points, resulting in the notable Hall current $\mathbf{j} \sim \mathbf{E} \times \mathbf{\Omega}$ in which \mathbf{E} refers to electric field.

Now we propose that the second harmonic generation (SHG) can distinguish between altermagnetic and ferromagnetic phases. The polarization of resultant light in

the SHG is defined as $P_i(2\omega) = \chi_{ijk} E_j(\omega) E_k(\omega)$, where E_j and E_k denote the electric field of incident light with frequency ω , and χ_{ijk} is SHG susceptibility. The SHG susceptibility is related to second order optical conductivity $\chi_{ijk} = i\sigma_{ijk}/2\epsilon_0\omega$. If spin orientation is along $\pm z$ direction, the symmetry analysis indicate that $\text{Im}\chi_{xyz} = \text{Im}\chi_{xzy} = -\text{Im}\chi_{yxz} = -\text{Im}\chi_{yzx}$ in the altermagnetic state, whereas in the ferromagnetic state, $\text{Im}\chi_{xyz} = \text{Im}\chi_{xzy} = \text{Im}\chi_{yxz} = \text{Im}\chi_{yzx}$ [63]. Thus, the magnetic transition and topological transition induced by external magnetic field or defect can be distinguished by SHG probe.

The altermagnets can provide the non-zero spin-splitter torque effect due to their anisotropic band splittings, which are absent in the conventional antiferromagnets. What do Dirac fermions bring to the altermagnets? The double degenerate bands near the Dirac fermions in the altermagnet contribute to the larger nonrelativistic spin current and enhanced spin-splitter torque compared to other altermagnet without electronic degeneracy. To quantify the charge-spin conversion ratio, we consider the spin conductivity with Kubo formula within constant scattering-rate Γ approximation. The spin conductivity σ_{bc}^a describes the spin- a current J_b^a along b direction under applied electric field along c direction. It can be split into the \mathcal{T} -odd part [64],

$$\sigma_{bc}^{\text{odd},a} = -\frac{e\hbar}{V\pi} \text{Re} \sum_{\mathbf{k}, m, n} \frac{\langle u_n(\mathbf{k}) | \hat{J}_b^a | u_m(\mathbf{k}) \rangle \langle u_m(\mathbf{k}) | \hat{v}_c | u_n(\mathbf{k}) \rangle \Gamma^2}{(E_F - E_n(\mathbf{k}))^2 + \Gamma^2 (E_F - E_m(\mathbf{k}))^2 + \Gamma^2}, \quad (2)$$

and \mathcal{T} -even part within the $\Gamma \rightarrow 0$ limit,

$$\sigma_{bc}^{\text{even},a} = \frac{2e\hbar}{V} \text{Im} \sum_{\mathbf{k}, m \neq n} \frac{\langle u_n(\mathbf{k}) | \hat{J}_b^a | u_m(\mathbf{k}) \rangle \langle u_m(\mathbf{k}) | \hat{v}_c | u_n(\mathbf{k}) \rangle}{(E_n(\mathbf{k}) - E_m(\mathbf{k}))^2}. \quad (3)$$

Here E_F is Fermi energy and \hat{v}_c is velocity operator. Our calculations reveal that \mathcal{T} -odd charge-spin conversion ratio of Ce_4Sb_3 reaches $\sim 10\%$ as shown in the Fig.S7, which is close to those of conventional altermagnets without topologically non-trivial fermions [64]. As for \mathcal{T} -even charge-spin conversion ratio, $\sigma_{bc}^{\text{even},a}/\sigma \rightarrow 0$ in the clean limit in the conventional altermagnet [64]. But $\sigma_{bc}^{\text{even},a}/\sigma$ in the Ce_4Sb_3 with Dirac fermions and CrSb with Weyl fermions [62] behave remarkable near the topologically non-trivial fermions as shown in the Fig.3(d). In this viewpoint, Dirac-fermion electronic structures in the altermagnets merge the advantages of altermagnets and Dirac fermions in the conventional antiferromagnets [57]. As for the nonlinear transport induced by quantum geometry in the altermagnet [65], the Dirac points denote additional interband contribution in the nonlinear transport.

In this work, we report the non-trivial topological

fermions in the altermagnet Ce_4Sb_3 . Our first-principles calculations, symmetry analysis and tight-binding model prove the 4-fold Dirac fermions in the altermagnetic state. When the altermagnetic states are transitioned into the ferromagnetic states, the topological transition occurs and 4-fold Dirac fermions are evolved into 6-fold degenerate fermions. The symmetry analysis shows that magnetic transition and topological transition can be probed by nonlinear optical experiments. The electronic doublet near the Dirac fermions can contribute to enhanced spin-splitting torque and strong nonlinear transport. Therefore, the Ce_4Sb_3 altermagnet serves as a promising platform for studying the interplay between topology and altermagnetism.

Acknowledge. We thank Xiaobing Chen for helpful discussions. This work was supported by the National Natural Science Foundation of China (No. 12304217) and the Fundamental Research Funds for the Central Universities from China.

* zhangshh@hnu.edu.cn

- [1] L. Šmejkal, J. Sinova, and T. Jungwirth, *Physical Review X* **12**, 031042 (2022).
- [2] L. Bai, W. Feng, S. Liu, L. Šmejkal, Y. Mokrousov, and Y. Yao, *arXiv preprint arXiv:2406.02123* (2024).
- [3] Y. Fang, L. Chen, and Q. Si, *arXiv preprint arXiv:2403.02295* (2024).
- [4] Z. Xiao, J. Zhao, Y. Li, R. Shindou, and Z.-D. Song, *arXiv preprint arXiv:2307.10364* (2023).
- [5] Y. Jiang, Z. Song, T. Zhu, Z. Fang, H. Weng, Z.-X. Liu, J. Yang, and C. Fang, *arXiv preprint arXiv:2307.10371* (2023).
- [6] X. Chen, J. Ren, J. Li, Y. Liu, and Q. Liu, *arXiv preprint arXiv:2307.12366* (2023).
- [7] J. Ren, X. Chen, Y. Zhu, Y. Yu, A. Zhang, J. Li, C. Li, and Q. Liu, *arXiv preprint arXiv:2307.10369* (2023).
- [8] Z.-F. Gao, S. Qu, B. Zeng, J.-R. Wen, H. Sun, P. Guo, and Z.-Y. Lu, *arXiv preprint arXiv:2311.04418* (2023).
- [9] S. Qu, Z.-F. Gao, H. Sun, K. Liu, P.-J. Guo, and Z.-Y. Lu, *arXiv preprint arXiv:2401.11065* (2024).
- [10] C.-Y. Tan, Z.-F. Gao, H.-C. Yang, K. Liu, P.-J. Guo, and Z.-Y. Lu, *arXiv preprint arXiv:2406.16603* (2024).
- [11] S.-D. Guo, Y. Liu, and C.-C. Liu, *arXiv preprint arXiv:2406.13950* (2024).
- [12] R. He, D. Wang, N. Luo, J. Zeng, K.-Q. Chen, and L.-M. Tang, *Physical Review Letters* **130**, 046401 (2023).
- [13] T. Okugawa, K. Ohno, Y. Noda, and S. Nakamura, *Journal of Physics: Condensed Matter* **30**, 075502 (2018).
- [14] O. Fedchenko, J. Minár, A. Akashdeep, S. W. D'Souza, D. Vasilyev, O. Tkach, L. Odenbreit, Q. Nguyen, D. Kutnyakhov, N. Wind, *et al.*, *Science Advances* **10**, eadj4883 (2024).
- [15] K.-H. Ahn, A. Hariki, K.-W. Lee, and J. Kuneš, *Physical Review B* **99**, 184432 (2019).
- [16] Z. Lin, D. Chen, W. Lu, X. Liang, S. Feng, K. Yamagami, J. Osiecki, M. Leandersson, B. Thiagarajan, J. Liu, *et al.*, *arXiv preprint arXiv:2402.04995* (2024).
- [17] T. Berlijn, P. C. Snijders, O. Delaire, H.-D. Zhou, T. A. Maier, H.-B. Cao, S.-X. Chi, M. Matsuda, Y. Wang, M. R. Koehler, *et al.*, *Physical review letters* **118**, 077201 (2017).
- [18] T. Tschirner, P. Keßler, R. D. Gonzalez Betancourt, T. Kotte, D. Kriegner, B. Büchner, J. Dufouleur, M. Kamp, V. Jovic, L. Šmejkal, *et al.*, *APL Materials* **11** (2023).
- [19] L. Šmejkal, A. Marmodoro, K.-H. Ahn, R. González-Hernández, I. Turek, S. Mankovsky, H. Ebert, S. W. D'Souza, O. Šipr, J. Sinova, *et al.*, *Physical Review Letters* **131**, 256703 (2023).
- [20] L.-D. Yuan, Z. Wang, J.-W. Luo, E. I. Rashba, and A. Zunger, *Physical Review B* **102**, 014422 (2020).
- [21] S. Bhowal and N. A. Spaldin, *Physical Review X* **14**, 011019 (2024).
- [22] Y.-X. Li, Y. Liu, and C.-C. Liu, *arXiv preprint arXiv:2404.14645* (2024).
- [23] I. I. Mazin, K. Koepernik, M. D. Johannes, R. González-Hernández, and L. Šmejkal, *Proceedings of the National Academy of Sciences* **118**, e2108924118 (2021).
- [24] S. Reimers, L. Odenbreit, L. Šmejkal, V. N. Strocov, P. Constantinou, A. B. Hellenes, R. Jaeschke Ubiergo, W. H. Campos, V. K. Bharadwaj, A. Chakraborty, *et al.*, *Nature Communications* **15**, 2116 (2024).
- [25] S. Reimers, L. Odenbreit, L. Šmejkal, V. N. Strocov, P. Constantinou, A. B. Hellenes, R. Jaeschke Ubiergo, W. H. Campos, V. K. Bharadwaj, A. Chakraborty, *et al.*, *Nature Communications* **15**, 2116 (2024).
- [26] T. Urata, W. Hattori, and H. Ikuta, *arXiv preprint arXiv:2403.19233* (2024).
- [27] M. Naka, S. Hayami, H. Kusunose, Y. Yanagi, Y. Motome, and H. Seo, *Nature communications* **10**, 4305 (2019).
- [28] M. Naka, S. Hayami, H. Kusunose, Y. Yanagi, Y. Motome, and H. Seo, *Physical Review B* **102**, 075112 (2020).
- [29] S.-D. Guo, X.-S. Guo, K. Cheng, K. Wang, and Y. S. Ang, *Applied Physics Letters* **123** (2023).
- [30] J. Söderquist and T. Olsen, *arXiv preprint arXiv:2401.05992* (2024).
- [31] M. Milivojević, M. Orozović, S. Picozzi, M. Gmitra, and S. Stavić, *arXiv preprint arXiv:2401.15424* (2024).
- [32] H.-Y. Ma, M. Hu, N. Li, J. Liu, W. Yao, J.-F. Jia, and J. Liu, *Nature communications* **12**, 2846 (2021).
- [33] S.-D. Guo, Y.-L. Tao, G. Wang, and Y. S. Ang, *Journal of Physics: Condensed Matter* (2024).
- [34] L. Šmejkal, A. H. MacDonald, J. Sinova, S. Nakatsuji, and T. Jungwirth, *Nature Reviews Materials* **7**, 482 (2022).
- [35] L. Šmejkal, J. Sinova, and T. Jungwirth, *Physical Review X* **12**, 040501 (2022).
- [36] D.-F. Shao, J. Ding, G. Gurung, S.-H. Zhang, and E. Y. Tsymlal, *Physical Review Applied* **15**, 024057 (2021).
- [37] L. Attias, A. Levchenko, and M. Khodas, *arXiv preprint arXiv:2402.12115* (2024).
- [38] L. Šmejkal, R. González-Hernández, T. Jungwirth, and J. Sinova, *Science advances* **6**, eaaz8809 (2020).
- [39] K. Samanta, M. Ležaić, M. Merte, F. Freimuth, S. Blügel, and Y. Mokrousov, *Journal of applied physics* **127** (2020).
- [40] R. G. Betancourt, J. Zubáč, R. Gonzalez-Hernandez, K. Geishendorf, Z. Šobán, G. Springholz, K. Olejník, L. Šmejkal, J. Sinova, T. Jungwirth, *et al.*, *Physical Review Letters* **130**, 036702 (2023).
- [41] K. Samanta, M. Ležaić, M. Merte, F. Freimuth, S. Blügel,

- and Y. Mokrousov, *Journal of Applied Physics* **127** (2020).
- [42] Q. Cui, B. Zeng, P. Cui, T. Yu, and H. Yang, *Physical Review B* **108**, L180401 (2023).
- [43] S. Hayami, Y. Yanagi, and H. Kusunose, *Journal of the Physical Society of Japan* **88**, 123702 (2019).
- [44] H. Bai, Y. Zhang, Y. Zhou, P. Chen, C. Wan, L. Han, W. Zhu, S. Liang, Y. Su, X. Han, *et al.*, *Physical Review Letters* **130**, 216701 (2023).
- [45] Y. Zhang, H. Bai, L. Han, C. Chen, Y. Zhou, C. H. Back, F. Pan, Y. Wang, and C. Song, *Advanced Functional Materials*, 2313332 (2024).
- [46] Y. Guo, J. Zhang, Z. Zhu, Y.-y. Jiang, L. Jiang, C. Wu, J. Dong, X. Xu, W. He, B. He, *et al.*, *Advanced Science*, 2400967 (2024).
- [47] Z. Feng, X. Zhou, L. Šmejkal, L. Wu, Z. Zhu, H. Guo, R. González-Hernández, X. Wang, H. Yan, P. Qin, *et al.*, *Nature Electronics* **5**, 735 (2022).
- [48] M. Naka, Y. Motome, and H. Seo, *Physical Review B* **103**, 125114 (2021).
- [49] X. Zhou, W. Feng, R.-W. Zhang, L. Šmejkal, J. Sinova, Y. Mokrousov, and Y. Yao, *Physical Review Letters* **132**, 056701 (2024).
- [50] R. Hoyer, R. Jaeschke-Ubiergo, K.-H. Ahn, L. Šmejkal, and A. Mook, *arXiv preprint arXiv:2405.05090* (2024).
- [51] I. Solov'yev, *Physical Review B* **55**, 8060 (1997).
- [52] S. Karube, T. Tanaka, D. Sugawara, N. Kadoguchi, M. Kohda, and J. Nitta, *Physical Review Letters* **129**, 137201 (2022).
- [53] H. Bai, L. Han, X. Feng, Y. Zhou, R. Su, Q. Wang, L. Liao, W. Zhu, X. Chen, F. Pan, *et al.*, *Physical Review Letters* **128**, 197202 (2022).
- [54] P.-J. Guo, Y. Gu, Z.-F. Gao, and Z.-Y. Lu, *arXiv preprint arXiv:2312.13911* (2023).
- [55] Y.-X. Li and C.-C. Liu, *Physical Review B* **108**, 205410 (2023).
- [56] D. S. Antonenko, R. M. Fernandes, and J. W. Venderbos, *arXiv preprint arXiv:2402.10201* (2024).
- [57] P. Tang, Q. Zhou, G. Xu, and S.-C. Zhang, *Nature Physics* **12**, 1100 (2016).
- [58] R. Nirmala, A. Morozkin, O. Isnard, and A. Nigam, *Journal of Magnetism and Magnetic Materials* **321**, 188 (2009).
- [59] A. Morozkin, R. Nirmala, O. Isnard, S. K. Malik, J. Yao, Y. Mozharivskyj, and S. Granovsky, *Intermetallics* **19**, 1794 (2011).
- [60] T. Suzuki, O. Nakamura, N. Tomonaga, S. Ozeki, Y. Kwon, A. Ochiai, T. Takeda, and T. Kasuya, *Physica B: Condensed Matter* **163**, 131 (1990).
- [61] M. Cococcioni and S. de Gironcoli, *Phys. Rev. B* **71**, 035105 (2005).
- [62] C. Li, M. Hu, Z. Li, Y. Wang, W. Chen, B. Thiagarajan, M. Leandersson, C. Polley, T. Kim, H. Liu, *et al.*, *arXiv preprint arXiv:2405.14777* (2024).
- [63] S. V. Gallego, J. M. Perez-Mato, L. Elcoro, E. S. Tasci, R. M. Hanson, K. Momma, M. I. Aroyo, and G. Madariaga, *Journal of Applied Crystallography* **49**, 1750 (2016).
- [64] R. González-Hernández, L. Šmejkal, K. Výborný, Y. Yahagi, J. Sinova, T. c. v. Jungwirth, and J. Železný, *Phys. Rev. Lett.* **126**, 127701 (2021).
- [65] Y. Fang, J. Cano, and S. A. A. Ghorashi, *Phys. Rev. Lett.* **133**, 106701 (2024).
- [66] G. Kresse and J. Furthmüller, *Physical Review B* **54**, 11169 (1996).
- [67] V. Wang, N. Xu, J.-C. Liu, G. Tang, and W.-T. Geng, *Computer Physics Communications* **267**, 108033 (2021).
- [68] J. P. Perdew, K. Burke, and M. Ernzerhof, *Physical Review Letters* **77**, 3865 (1996).
- [69] J. Gao, Q. Wu, C. Persson, and Z. Wang, *Computer Physics Communications* **261**, 107760 (2021).
- [70] X. He, N. Helbig, M. J. Verstraete, and E. Bousquet, *Computer Physics Communications* **264**, 107938 (2021).
- [71] T. Holstein and H. Primakoff, *Physical Review* **58**, 1098 (1940).

Supplementary Materials

Calculation methods

The first-principles calculations were performed using the Vienna Ab-initio Simulation Package (VASP) based on density functional theory (DFT)[66, 67]. The Perdew-Becke-Ernzerhof (PBE) functional with generalized gradient approximation (GGA)[68] is adopt to describe the exchange-correlated potential. The cutoff energy of the plane-wave is 410 eV, and Brillouin zone is sampled by a $8 \times 8 \times 8$ mesh. The irreducible representation of wave-functions are calculated by irvsp[69] code. We calculated different exchange couplings by Green function method as implemented in TB2J package[70].

The spin-wave Hamiltonian

Here we only consider the nearest neighboring exchange couplings.

$$\hat{H} = -J_1 \sum_{\langle i,j \rangle} \hat{S}_i^{A/B} \cdot \hat{S}_j^{A/B} - J_2 \sum_{\langle i,j \rangle} \hat{S}_i^{A/B} \cdot \hat{S}_j^{B/A} \quad (4)$$

where J_1 is the same sublattice (A or B) exchange, and J_2 is the exchange parameter between the different sublattice. We can write spin operators $\hat{S}_i^{A/B} = \hat{S}_i^{A/B,x} \hat{x} + \hat{S}_i^{A/B,y} \hat{y} + \hat{S}_i^{A/B,z} \hat{z}$ for A/B sublattices in cartesian coordinates. The Holstein-Primakoff (HP) transformation[71] can replace the spin operator in the

formula (4) with the boson operator.

$$\begin{aligned} \hat{S}_i^{A,+} &= \sqrt{2S - \hat{a}_i^+ \hat{a}_i} \hat{a}_i, & \hat{S}_i^{A,-} &= \sqrt{2S - \hat{a}_i^+ \hat{a}_i} \hat{a}_i^+ \\ \hat{S}_i^{A,z} &= S - \hat{a}_i^+ \hat{a}_i, \\ \hat{S}_j^{B,+} &= \sqrt{2S - \hat{b}_j^+ \hat{b}_j} \hat{b}_j^+, & \hat{S}_j^{B,-} &= \sqrt{2S - \hat{b}_j^+ \hat{b}_j} \hat{b}_j \\ \hat{S}_j^{B,z} &= \hat{b}_j^+ \hat{b}_j - S. \end{aligned} \quad (5)$$

The $\hat{a}_i^\dagger (\hat{b}_j^\dagger)$ and $\hat{a}_i (\hat{b}_j)$ correspond to the bosonic creation and annihilation operators, respectively. And $\hat{S}^{A/B,\pm} = \hat{S}^{A/B,x} \pm i \hat{S}^{A/B,y}$. In the low-excited state, only few spins are deflected, and the average deviation of each spin is small, so $\sqrt{2S}$ can be used instead of the square root of HP transformation, and the fourth order term of the operator is omitted. Then we can make the Fourier transformation

$$\begin{aligned} \hat{a}_i^\dagger / \hat{b}_i &= \frac{1}{\sqrt{N}} \sum_k e^{-ik \cdot r_i} \hat{a}_k^\dagger / \hat{b}_k \\ \hat{a}_i / \hat{b}_i &= \frac{1}{\sqrt{N}} \sum_k e^{ik' \cdot r_i} \hat{a}_{k'} / \hat{b}_{k'} \end{aligned} \quad (6)$$

Here $\hat{a}_k^\dagger (\hat{b}_k^\dagger)$ and $\hat{a}_k (\hat{b}_k)$ satisfy the bosonic commutation relation $[\hat{a}_k, \hat{a}_{k'}^\dagger] = [\hat{b}_k, \hat{b}_{k'}^\dagger] = \delta_{kk'}$. Combining Ce atomic coordinate Table(S1) and formula(5), (6), we get momentum-space Hamiltonian. Using $\Psi_+ = (\hat{a}_k^+, \hat{b}_k)$ or $\Psi_- = (\hat{b}_k^+, \hat{a}_k)$ spinor basis, the spin-wave Hamiltonian can be written as

$$\hat{H}_{k,\pm} = \begin{pmatrix} A_k \pm \Delta_k & B_k - iD_k \\ B_k + iD_k & A_k \mp \Delta_k \end{pmatrix} \quad (7)$$

Here A_k , Δ_k , B_k and D_k terms are

$$\begin{aligned} A_k &= 4J_1 S - 8J_2 S - 2J_1 S [\cos 2ax k_x \cos(a + 2ax)k_y + \cos(a + 2ax)k_x \cos 2ax k_y] \\ \Delta_k &= 2J_1 S [\sin 2ax k_x \sin(a + 2ax)k_y + \sin(a + 2ax)k_x \sin 2ax k_y] \\ B_k &= -2J_1 S [\cos 2ax k_y \cos(a + 2ax)k_z + \cos(a + 2ax)k_x \cos 2ax k_z + \cos 2ax k_z \cos(a + 2ax)k_y + \cos(a + 2ax)k_z \cos 2ax k_x] \\ D_k &= 2J_1 S [\sin(a + 2ax)k_z \cos 2ax k_y + \sin 2ax k_z \cos(a + 2ax)k_y + \cos(a + 2ax)k_x \sin 2ax k_z + \sin(a + 2ax)k_z \cos 2ax k_x]. \end{aligned} \quad (8)$$

The Hamiltonian (7) can be diagonalized with $T_k^\dagger H_{k,+} T_k = \text{diag}(E_{k,\alpha}, E_{-k,\beta})$ and $T_k^\dagger H_{k,-} T_k = \text{diag}(E_{k,\beta}, E_{-k,\alpha})$ [50]. The eigenvalues are as follows

$$\begin{aligned} E_{k,\alpha} &= \epsilon_k + \Delta_k, & E_{k,\beta} &= \epsilon_k - \Delta_k \\ \epsilon_k &= \sqrt{A_k^2 - B_k^2 - D_k^2} \end{aligned} \quad (9)$$

The frequency difference between spin-wave branches is proportional to Δ_k . When k_x or $k_y = 0$, two branches are degenerate as shown in the calculated magnon dispersion in the Fig.S1. Because Δ_k is the odd function

of k_x or k_y , two magnon branches exhibit chiral splitting when $k_x k_y \neq 0$. But it should be noted that high Gilbert damping present in this metallic antiferromagnet makes it challenging to detect the chiral splitting in experiments.

The symmetry protection

We use $\{C_{2y} \tau_x | \mathcal{T}\}$ to elaborate how the Ce atom is spatially transformed within the unit cell. Firstly, we

replace the fractional coordinates of the Ce atom in Ta-

ble. S1 with Cartesian coordinates as follows.

$$\begin{aligned}
Ce1 : (ax, ax, ax) &\xrightarrow{C_{2y}\tau} (-ax, ax, -ax) \xrightarrow{\tau_x} Ce3 : (a - ax, ax, -ax) \\
Ce2 : (ax, -ax, a(1-x)) &\xrightarrow{C_{2y}\tau} (-ax, -ax, ax - a) \xrightarrow{\tau_x} Ce4 : (-ax, a - ax, ax) \\
Ce5 : (\frac{a}{2} + ax, \frac{a}{2} + ax, \frac{a}{2} + ax) &\xrightarrow{C_{2y}\tau} (-\frac{a}{2} - ax, \frac{a}{2} + ax, -\frac{a}{2} - ax) \xrightarrow{\tau_x} Ce8 : (\frac{3a}{2} - ax, ax - \frac{a}{2}, \frac{a}{2} - ax) \\
Ce6 : (-\frac{a}{2} + ax, \frac{a}{2} - ax, \frac{3a}{2} - ax) &\xrightarrow{C_{2y}\tau} (\frac{a}{2} - ax, \frac{a}{2} - ax, ax - \frac{3a}{2}) \xrightarrow{\tau_x} Ce7 : (\frac{a}{2} - ax, \frac{3a}{2} - ax, -\frac{a}{2} + ax)
\end{aligned} \tag{10}$$

Here we summarize the symmetric operators in the Table. S1.

TABLE S1. The fractional coordinates of Ce atoms in the primitive cell. Here the basis vectors of primitive cell are $\mathbf{a}_1 = (-a, a, a)$, $\mathbf{a}_2 = (a, -a, a)$, $\mathbf{a}_3 = (a, a, -a)$. The lattice constant is $\sqrt{3}a = 8.316\text{\AA}$. And the transformations under $M_{yz}C_{4z}\tau'$ operation and $C_{2y}\tau_x$ operation are listed. For example, the site 1 is transformed into site 7 under $M_{yz}C_{4z}\tau'$ operation. Under $C_{2y}\tau_x$ operation, the site 1 is transformed into site 3.

Atomic index	Fractional coordinates	spin	$M_{yz}C_{4z}\tau'$	$C_{2y}\tau_x$
Ce1	(x, x, x)	\downarrow	Ce7	Ce3
Ce2	$(\frac{1}{2} - x, \frac{1}{2}, 0)$	\uparrow	Ce6	Ce4
Ce3	$(0, \frac{1}{2} - x, \frac{1}{2})$	\uparrow	Ce8	Ce1
Ce4	$(\frac{1}{2}, 0, \frac{1}{2} - x)$	\downarrow	Ce5	Ce2
Ce5	$(\frac{1}{2} + x, \frac{1}{2} + x, \frac{1}{2} + x)$	\downarrow	Ce4	Ce8
Ce6	$(1 - x, \frac{1}{2}, 0)$	\uparrow	Ce2	Ce7
Ce7	$(\frac{1}{2}, 0, 1 - x)$	\downarrow	Ce1	Ce6
Ce8	$(0, 1 - x, \frac{1}{2})$	\uparrow	Ce3	Ce5

Along the Γ - H_y direction ($k_x = k_z = 0$), the wave function obey the symmetry $\{C_{2y}\tau_x|\mathcal{T}\}$. Under symmet-

ric operation $\{C_{2y}\tau_x|\mathcal{T}\}$, (x, y, z) is transited into $(-x - 1/2, y, -z)$, and (k_x, k_y, k_z) becomes $(k_x, -k_y, k_z)$. Under $M_{yz}C_{4z}\tau'$ operation, (x, y, z) becomes $(-y - 1/4, -x + 1/4, z - 1/4)$, and the H-N direction satisfying $k_x + k_y = 0$ obeys this symmetric operation.

TABLE S2. The energy differences $\Delta E = E_{AFM} - E_{FM}$ calculated with different U parameters.

U(eV)	ΔE (eV)
0	0.26879
1	-0.71818
2	-2.83711
3	-4.57766
4	0.25884
5	0.23083
6	0.20625
7	0.18279

The tight-binding model

Now we use the eight-atom tight-binding model to describe the electronic structure of nonmagnetic state. Each atom has three nearest neighboring sites, so the tight-binding Hamiltonian can be written as

$$H_0 = \begin{bmatrix} E_0 & t_0 e^{i\mathbf{k}\cdot\mathbf{r}_{21}} & t_0 e^{i\mathbf{k}\cdot\mathbf{r}_{31}} & t_0 e^{i\mathbf{k}\cdot\mathbf{r}_{41}} & 0 & 0 & 0 & 0 \\ t_0 e^{i\mathbf{k}\cdot\mathbf{r}_{12}} & E_0 & t_0 e^{i\mathbf{k}\cdot\mathbf{r}_{32}} & t_0 e^{i\mathbf{k}\cdot\mathbf{r}_{42}} & 0 & 0 & 0 & 0 \\ t_0 e^{i\mathbf{k}\cdot\mathbf{r}_{13}} & t_0 e^{i\mathbf{k}\cdot\mathbf{r}_{23}} & E_0 & t_0 e^{i\mathbf{k}\cdot\mathbf{r}_{43}} & 0 & 0 & 0 & 0 \\ t_0 e^{i\mathbf{k}\cdot\mathbf{r}_{14}} & t_0 e^{i\mathbf{k}\cdot\mathbf{r}_{24}} & t_0 e^{i\mathbf{k}\cdot\mathbf{r}_{34}} & E_0 & 0 & 0 & 0 & 0 \\ 0 & 0 & 0 & 0 & E_0 & t_0 e^{i\mathbf{k}\cdot\mathbf{r}_{65}} & t_0 e^{i\mathbf{k}\cdot\mathbf{r}_{75}} & t_0 e^{i\mathbf{k}\cdot\mathbf{r}_{85}} \\ 0 & 0 & 0 & 0 & t_0 e^{i\mathbf{k}\cdot\mathbf{r}_{56}} & E_0 & t_0 e^{i\mathbf{k}\cdot\mathbf{r}_{76}} & t_0 e^{i\mathbf{k}\cdot\mathbf{r}_{86}} \\ 0 & 0 & 0 & 0 & t_0 e^{i\mathbf{k}\cdot\mathbf{r}_{57}} & t_0 e^{i\mathbf{k}\cdot\mathbf{r}_{67}} & E_0 & t_0 e^{i\mathbf{k}\cdot\mathbf{r}_{87}} \\ 0 & 0 & 0 & 0 & t_0 e^{i\mathbf{k}\cdot\mathbf{r}_{58}} & t_0 e^{i\mathbf{k}\cdot\mathbf{r}_{68}} & t_0 e^{i\mathbf{k}\cdot\mathbf{r}_{78}} & E_0 \end{bmatrix}. \tag{11}$$

In the ferromagnetic state, the tight-binding model becomes 16-band model as following

$$H_{FM} = (H_0 + H_m) \bigoplus (H_0 - H_m) \tag{12}$$

Here H_m is the Zeeman term

$\text{diag}\{m, m, m, m, m, m, m, m\}$. Then we can obtain two sextuple degenerate solutions $E_0 + t \pm m$ and two two-fold degenerate solutions $E_0 - 3t \pm m$ at the H point.

As for the antiferromagnetic state, the Zeeman term H_m in the tight-binding model becomes $H_m =$

$\text{diag}\{m, -m, -m, m, m, -m, m, -m\}$. At the H point, the eigenvalues become

$$\begin{aligned}
 E_1 &= E_0 - t + \sqrt{m^2 + 4t^2} \quad (\text{four-fold}) \\
 E_2 &= E_0 - t - \sqrt{m^2 + 4t^2} \quad (\text{four-fold}) \\
 E_3 &= E_0 + t + m \quad (\text{four-fold}) \\
 E_4 &= E_0 + t - m \quad (\text{four-fold})
 \end{aligned} \tag{13}$$

TABLE S3. List of the character table of point group D_{2d} by using irvsp code at H point of AFM state.

representation	E	2IC ₄	C ₂	2C ₂	2IC ₂
H ₁	1	1	1	1	1
H ₂	1	1	1	-1	-1
H ₃	1	-1	1	1	-1
H ₄	1	-1	1	-1	1
H ₅	2	0	-2	0	0

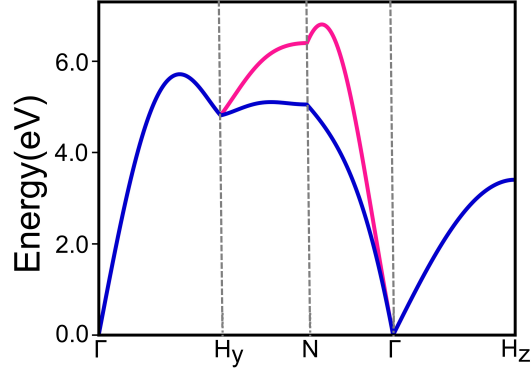


FIG. S1. The chiral splitting magnon spectrum with only considering nearest neighboring exchange couplings $J=-0.43$ eV. The blue (red) line corresponds to different magnon branches. Here H_y and H_z points refer to $(0, \pi/a, 0)$ and $(0, 0, \pi/a)$, respectively.

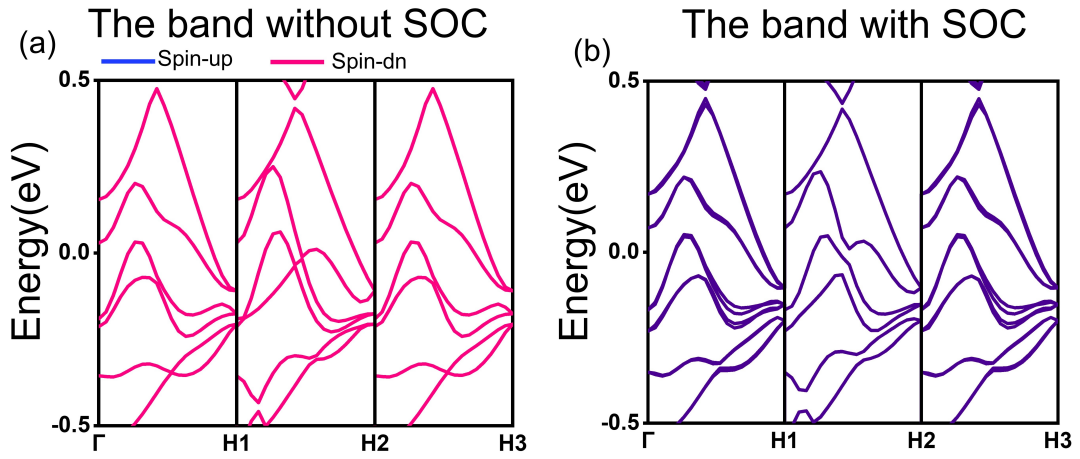


FIG. S2. (a) The electronic band structure of the Ce_4Sb_3 compound without SOC in the AFM at $U=2$ eV, where the blue lines represent the spin-up bands and the red lines represent the spin-down bands. (b) The electronic band structure of Ce_4Sb_3 with SOC in the AFM at $U=2$ eV.

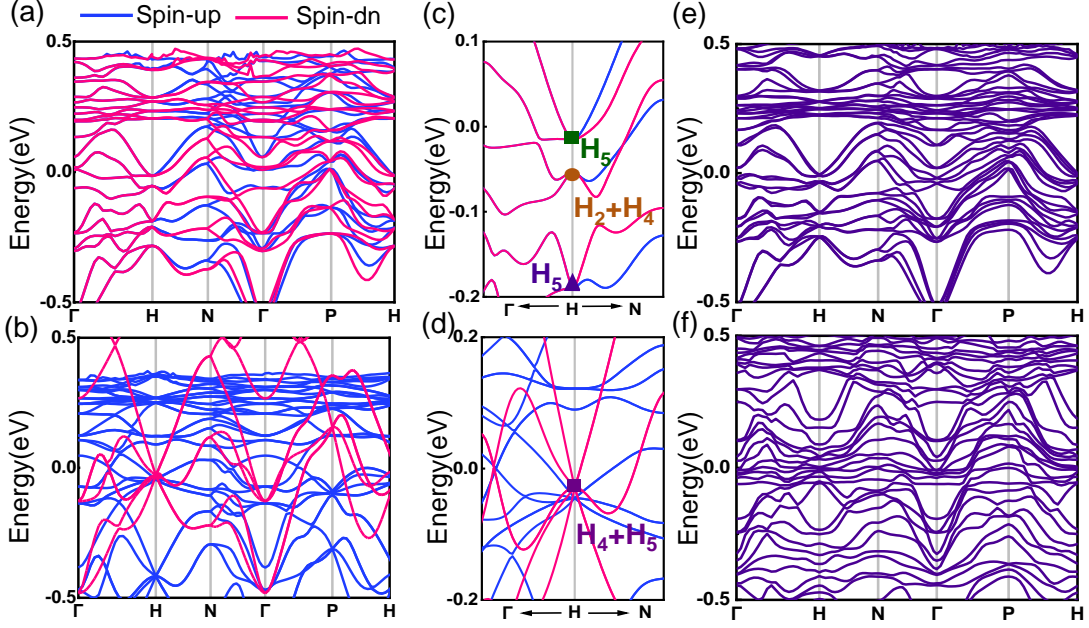


FIG. S3. At $U=1$ eV, the electronic band structure and irreducible representation of the Ce_4Sb_3 compound, where the blue lines represent the spin-up bands and the red lines represent the spin-down bands. (a) Band structure of the AFM state without SOC. (b) Band structure of the FM state without SOC. (c) Irreducible representation of the AFM state at quadruple degenerate points. (d) Irreducible representation of the FM state at sextuple degenerate points. (e) Band structure of the AFM state with SOC. (f) Band structure of the FM state with SOC.

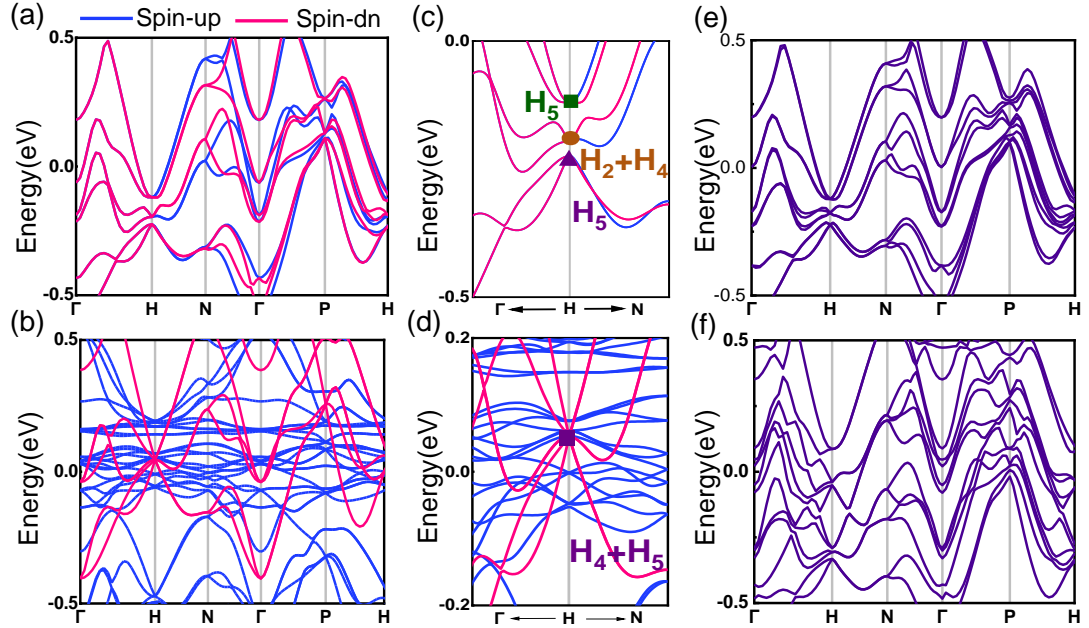


FIG. S4. At $U=3$ eV, the electronic band structure and irreducible representation of the Ce_4Sb_3 compound, where the blue lines represent the spin-up bands and the red lines represent the spin-down bands. (a) Band structure of the AFM state without SOC. (b) Band structure of the FM state without SOC. (c) Irreducible representation of the AFM state at quadruple degenerate points. (d) Irreducible representation of the FM state at sextuple degenerate points. (e) Band structure of the AFM state with SOC. (f) Band structure of the FM state with SOC.

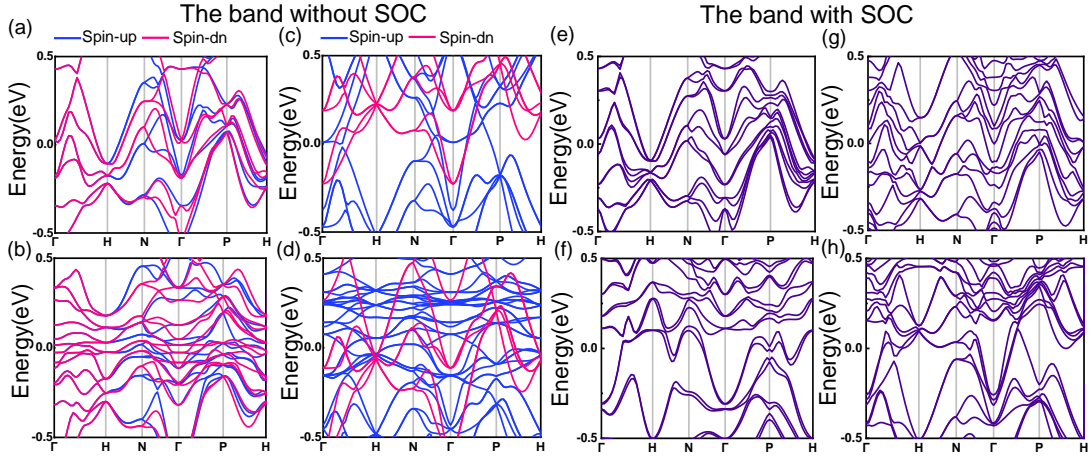


FIG. S5. The band structure of the Ce_4Bi_3 compound in the first row and the Ce_4As_3 compound in the second row, where the blue line represents the spin up and the red line represents the spin down. (a)-(b) Band structure of AFM state without SOC. (c)-(d) Band structure of FM state without SOC. (e)-(f) Band structure of AFM state with SOC. (g)-(h) Band structure of FM state with SOC.

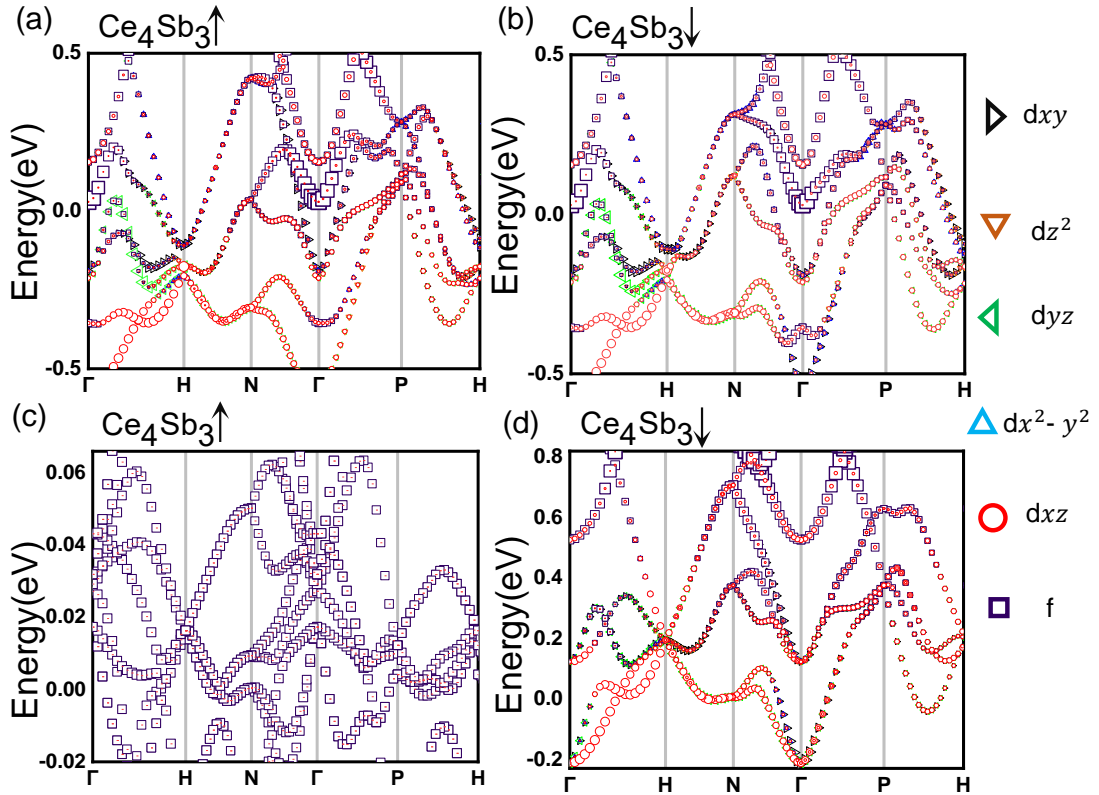


FIG. S6. At $U=2$ eV, orbital resolved energy bands of the Ce_4Sb_3 compound without SOC effect. (a) and (b) figures represent the AFM state. (c) and (d) figures refer to the FM state.

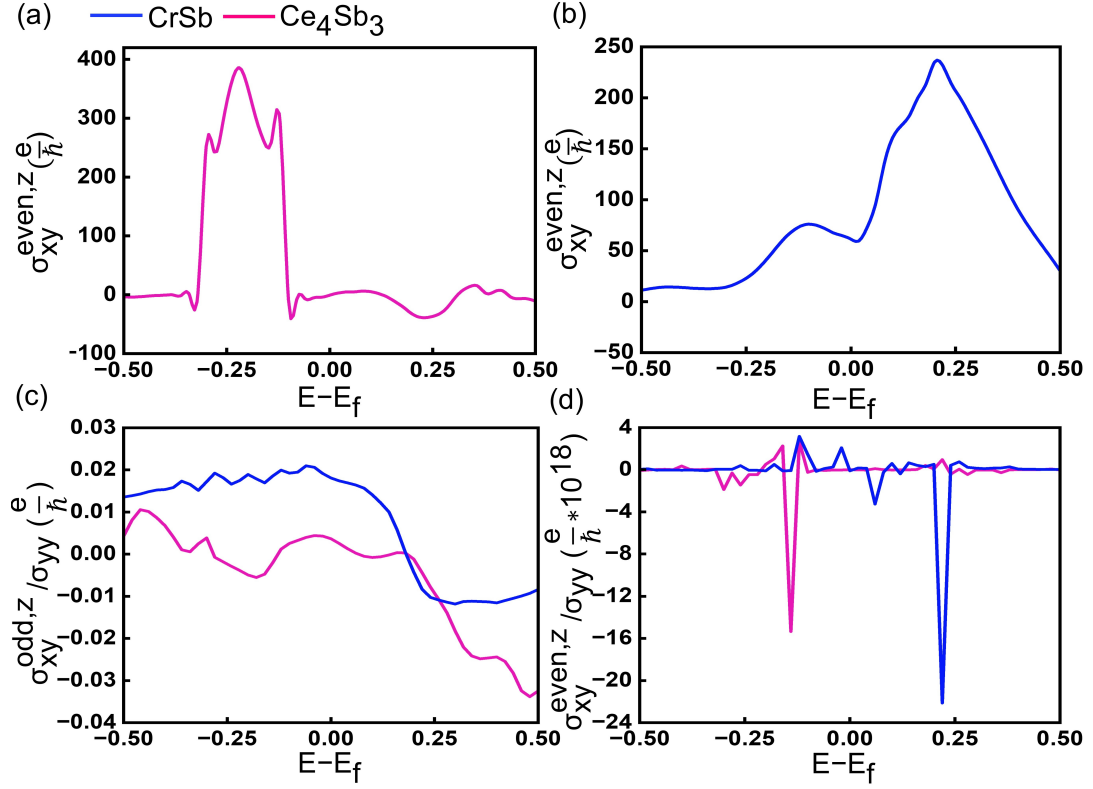


FIG. S7. The calculated Spin conductivity and spin current angle of the Ce_4Sb_3 compound and CrSb , where the blue lines represent the CrSb and the red lines refer to the Ce_4Sb_3 with the SOC effect. (a) \mathcal{T} -even spin Hall conductivity of the Ce_4Sb_3 compound. (b) \mathcal{T} -even spin Hall conductivity of the CrSb compound. (c) \mathcal{T} -odd charge-spin conversion ratio as a function of the scattering rate. (d) \mathcal{T} -even spin charge-spin conversion ratio.